Contents lists available at ScienceDirect

Journal of Magnetism and Magnetic Materials

journal homepage: www.elsevier.com

Research articles

Magnetic and power absorption measurements on iron oxide nanoparticles synthesized by thermal decomposition of $Fe(acac)_3$

N. Jović Orsini[a,*], B. Babić-Stojić[a], V. Spasojević[a], M.P. Calatayud[b], N. Cvjetićanin[c], G.F. Goya[b]

[a] Vinča Institute of Nuclear Sciences (020), University of Belgrade, P.O. Box 522, RS-11001 Belgrade, Serbia
[b] Instituto de Nanociencia de Aragón and Departamento de Fisica de la Materia Condensada, Universidad de Zaragoza, Mariano Esquillor s/n 500018, Zaragoza, Spain
[c] Faculty of Physical Chemistry, University of Belgrade, Studentski trg 12-16, 11158 Belgrade 118, Serbia

ARTICLE INFO

Keywords:
Thermal decomposition method
Magnetic hyperthermia
Specific absorption rate
Néel relaxations

ABSTRACT

Iron oxide magnetic nanoparticles with diameters d, $7\,nm \le d \le 12\,nm$, were synthesized by thermal decomposition of $Fe(acac)_3$. Different experimental conditions, keeping constant concetration of Fe ions in solvent, showed that the heating rates is the most important parameter determining the final particle size. Use of two different solvents, *1*-eicosene and *1*-octadecene, yielded similar nanoparticle sizes ($7.1\,nm \le d \le 7.5\,nm$), but different magnetic anisotropies. All samples were superparamagnetic at room temperature. Spin disordering was inferred in samples coated with trioctylphosphine oxide (TOPO) co-ligand in addition to oleic acid and oleyamine. The heating ability of ~12 nm-sized nanoparticles dispersed in hexane under alternating magnetic fields ($3.98\,kA/m \le H_0 \le 23.87\,kA/m$; $229.3\,kHz \le f \le 828\,kHz$) has been studied, finding a nearly quadratic dependence upon H_0, as expected from the linear response theory.

1. Introduction

One of the promising techniques in cancer treatment, aside drug therapy, is magnetic hyperthermia [1–3]. This clinical protocol is based on the idea to induce tumor cells death by locally increasing the temperature of ill tissue, when they are previously loaded with magnetic nanoparticles (MNPs) and exposed to alternating (AC) magnetic field [4–6]. The underlying physical process is governed by the transformation of magnetic to thermal energy in each single-domain MNP through Brownian and Néel relaxation processes. The amount of generated heat power depends on the experimental conditions (field amplitude, H_0 and frequency, f), as well as on physical parameters of a system such as: viscosity of a medium, the chemical composition of MNPs, particle size and shape, the effective anisotropy of material, size and anisotropy dispersion, the interparticle interactions [7–12].

Nanoparticles of magnetite (Fe_3O_4) or maghemite (γ-Fe_2O_3) are among the most studied systems for this purpose due to their low toxicity for the human body [13–16]. There is some controversy about the optimum size and shape of iron oxide nanoparticles for maximum heating, and this is probably related to the fact that detailed models incorporating clustering effects, dipolar interactions and the more realistic mathematical Landau-Lifshitz-Gilbert equation to describe relaxation modes are still lacking. From the experimental point of view, it was found that Fe_3O_4 nanoparticles of ~15–25 nm size result in good heating rates under physiologically relevant AC magnetic field conditions [17,18]. Alternative approaches and systems, such as perovskite-based nanoparticles (with T_C in the range 13–82 °C) have also been investigated [19], as well as some core-shell structures and exchange-bias-coupled nanoparticles [20,21]. Finally, other ferromagnetic nanoparticles (e.g. FeCo or FePt alloys) [22,23] have been studied as potential heating mediators. Investigations on such systems can be interesting from the fundamental point of view, but their use can be limited by the biocompatibility.

In order to obtain ferrofluid with the best magnetic hyperthermia performances, different synthesis methods have been tested [24–26]. Well crystallized NPs, with narrow particle size distribution and the size close to the critical one determined by the transition from superparamagnetic (SPM) to ferromagnetic state, are desired. High-temperature decomposition of iron salts in organic media is a quite well known method for production of well crystallized iron oxide nanoparticles with narrow size distribution [27–33]. The main drawback of this non-

* Corresponding author.
Email address: natasaj@vin.bg.ac.rs (N.Jović Orsini)

https://doi.org/10.1016/j.jmmm.2017.10.053
Received 28 June 2017; Received in revised form 22 September 2017; Accepted 13 October 2017
Available online xxx
0304-8853/

green synthesis method is that nanocrystals are passivated with hydrophobic ligands that hinder their bioapplications. To make them biocompatible, the transformation from nonpolar to polar medium has to be done. It is possible through ligand exchange or ligand addition reactions in solution [34–36]. Unfortunately, these processes can bring to significant aggregation of NPs, their partial oxidation and disruption of heating capability. These issues should be properly resolved.

To investigate how the heating ability of NPs depends upon size, shape, degree of aggregation, surface functionalization and magnetic interparticle interactions, both, theoretical and experimental approaches are used [35,37–41]. Some studies are focused on the evolution of the heating efficiency of NPs with their size [9,12,42], and the others on the influence of shape and coating of NPs [32,43,44]. Slight deviation from the expected chemical composition can also influence heating ability of nanoparticles dispersed in a fluid, as well as the oxidation process which can take place and, thus hinder the stability of magnetic fluids in time [45,46]. Some recent studies have revealed that type of surfactant molecule, used to stabilize the surface of nanoparticles, can be important in determining the resulting crystal and magnetic structure of nanoparticles [45,47]. It has also been shown that the ligand exchange process can invoke changes of the magnetic ordering in the surface layer and consequently change the surface anisotropy contribution to the effective anisotropy constant [47]. Influence of dipolar interactions on the heating ability diverges. It can be noticed either the decrease or the increase of the heating power due to interactions [35,48].

In this paper, single crystalline iron oxide nanoparticles were synthesized using thermal decomposition of iron(III) acetylacetonate. The effects of different reaction conditions on the structural and magnetic properties of nanocrystals were examined. The hyperthermic properties of superparamagnetic iron oxide nanoparticles were investigated too. For the ferrofluid with nanoparticles ~12 nm in size and with a narrow size distribution, the measurements of the specific absorption rate (*SAR*) were performed in a wide range of experimental conditions: the amplitude, H_0 and the frequency, f of applied AC magnetic field. We have found *quadratic* field and frequency dependence of the *SAR*. On the contrary, de la Presa et al. [43] obtained the nearly quadratic f-dependence of the *SAR* in NPs around 8 nm in size, but not in the systems of bigger NPs with an average size around 11 and 13 nm. Therefore, we discussed our result taking into account value of the magnetic anisotropy constant. A ligand exchange process was performed on selected nanoparticles in a bipolar solvent using *meso-2,3*-dimercaptosuccinic acid (DMSA) molecules. Experimental results obtained for thus modified nanoparticles are presented in the Supplementary Information (SI)).

2. Experimental

2.1. Synthesis of magnetic iron oxide nanoparticles

Iron oxide nanocrystals were synthesized by thermal decomposition of iron acetylacetonate ($Fe(acac)_3$), in two different solvents, *1*-octadecene (boiling point ~315 °C) and *1*-eicosene (boiling point ~341 °C). The classical protocol during synthesis was followed [27]. A mixture of oleic acid (OA, $C_{17}H_{33}COOH$), oleylamine (OM, $C_{18}H_{35}NH_2$) and *1,2*-dodecandiol (*1,2*-DDDO, $C_{12}H_{26}O_2$) was added into a round bottom three neck flask, previously filled with: *i*) *1*-octadecene (samples $\mathbf{S_0}$ and $\mathbf{T_0}$), or *ii*) *1*-eicosene (sample $\mathbf{E_0}$). In the sample $\mathbf{T_0}$, co-ligand trioctylphosphine oxide (TOPO, $[CH_3(CH_2)_7]_3PO$) was used together with oleic acid (OA) with a molar ratio OA:TOPO = 3:1. The sample $\mathbf{SS_0}$ was obtained by a seed-mediated procedure using $\mathbf{S_0}$ nanocrystals as seeds. The sample $\mathbf{TT_0}$ was obtained by size sorting of the sample $\mathbf{T_0}$. All relevant parameters in synthesis: the molar ratio of reagents, the heating rates, the aging temperatures and the aging time, are given in Table 1. Detailed description of synthesis is given for the samples $\mathbf{S_0}$ and $\mathbf{SS_0}$ (see *Supplementary Information*).

2.2. Characterization

The mean particle size, polydispersity and morphology of as synthesized iron oxide nanoparticles were examined by a transmission electron microscope (TEM, FEI TECNAI T20, 200 kV). In order to determine the mean particle size, $<d>_{TEM}$, and the standard deviation σ, at least 350 particles were considered and data were fitted to a log-normal distribution.

The X-ray diffraction (XRD) pattern of the samples was collected using Rigaku SmartLab diffractometer equipped with Cu Kα radiation sources ($\lambda = 1.5418$ Å), operating at 40 kV and 30 mA. The data were recorded in the 2θ range from 10° to 80° with a step 0.02° and a counting time of 2 s per step.

The hydrodynamic size of iron oxide nanoparticles was studied by dynamic light scattering (DLS) method. DLS was performed with N5 Submicron Particle Size Analyzer (Beckman Couter, Inc.), in unimodal size mode, with detector at angle of 90° from the incident beam, and a time step of 60 s.

Field and temperature dependent magnetic measurements M(H) and M(T), were performed on as-prepared samples $\mathbf{S_0}$, $\mathbf{E_0}$, $\mathbf{T_0}$ and $\mathbf{SS_0}$ using a commercial superconducting quantum interference device (SQUID) magnetometer. To evaluate the weight of magnetic $\mathbf{S_0}$, $\mathbf{E_0}$, $\mathbf{T_0}$ and $\mathbf{SS_0}$ phase inside organics, the thermogravimetric analysis (TGA) and the differential thermal analysis (DTA) were employed using a TA SDT 2960 instrument (in air, at a heating rate of 10 °C/min, up to 650 °C), yielding a residue corresponding to 15.07, 9.62, 7.05 and 3.78 wt% of the original weight, respectively (see SI). Hysteresis loops, M(H), were recorded at 5 and 300 K at DC magnetic field up to 3978.88 kA/m (50 kOe). Field-cooled (FC) and zero-field-cooled (ZFC) DC magnetization measurements were performed in a magnetic field of 7.96 kA/m (100 Oe) following standard protocol.

To determine concentration of iron ions in the ferrofluids, UV-visible spectrometer (VARIAN, Cary 50 Probe) was used. The absorbance value of solutions was measured under irradiation of λ = 478 nm. Iron standard solution (1 mg/ml Fe in 2% HNO_3, Acros organics) was used to prepare patron solutions with different concentrations of Fe^{3+} ions in a mixture of 6M H_2SO_4 and 65% HNO_3. A calibration curve is obtained by fitting the absorbance of patron solutions *vs.* the concentration of Fe^{3+} ion in the range 1–5 μg of Fe^{3+}/ml. The concentration of iron in the samples was calculated using the calibration curve and the measured absorbance of the sample.

2.3. Measurements of specific absorption rate (SAR)

To compare the heating efficiency of iron oxide nanoparticles, the *SAR* of all samples dispersed in hexane ($\mathbf{S_0}$, $\mathbf{E_0}$, $\mathbf{T_0}$, $\mathbf{SS_0}$, and $\mathbf{TT_0}$) was measured in a commercial AC magnetic field applicator (model DM100 by nBnanoscale Biomagnetics). The ferrofluids were placed in a 2 ml glass holder and exposed to an alternating magnetic field, $H = H_0 \sin(\omega t)$. Then, the temperature *versus* time curve, T(t), was recorded under different experimental conditions: frequency, $f = \omega/2\pi$, and the magnetic field amplitude, H_0, keeping the adiabatic experimental conditions. Every sample solution was sonicated for at least 30 s before being used in measurements. From the initial slope of T(t) curve (approximated by a linear increase), a maximum rise of temperature in time, $(\partial T/\partial t)_{max}$, was extracted and used to obtain the *SAR* of ferrofluids, ac-

Table 1
The reaction parameters during thermal decomposition of $Fe(acac)_3$ salt: molar ratio of reactants; $\Delta T_1/\Delta t_1$ - initial heating rate, T_{1max} – temperature at first ramp, t_{1aging} – aging time at T_{1max}, $\Delta T_2/\Delta t_2$ - heating rate up to boiling point of solvent, T_{2max} – experimentally reached temperature during boiling of solvent, t_{2aging} – aging time at T_{2max}; $<d>_{TEM}$ – mean diameter of particles determined from TEM images (σ - relative width of the log-normal function); d_{hyd} – hydrodynamic diameter; *SAR* - specific absorption rate measured under conditions ($H_0 = 23.87$ kA/m (300 Oe), $f = 580.5$ kHz).

Sample	Fe:OA:OM: *1,2*-DDDO (:TOPO)	T_{1max} [°C]	$\Delta T_1/\Delta t_1$ [°C/min]	t_{1aging} [min]	T_{2max} [°C]	$\Delta T_2/\Delta t_2$ [°C/min]	t_{2aging} [min]	$<d>_{TEM}$ (σ) [nm]	d_{hyd} [nm]	SAR [W/g]
S_0	1:5:5:5	204(2)	1.5	120	290	1.7	30	7.1 (0.08)	59	15.1
E_0	1:3:3:5	203(3)	2	120	324–331	1.9	30	7.5 (0.05)	156	27.1
T_0	1:3:3:5(:1)	201(2)	3.4	120	319–329	5.1	50	8.8 (0.16)[a]	84[a]	80.7[a]
TT_0	1:3:3:5(:1)	201(2)	3.4	120	319–329	5.1	50	11.6 (0.07)	510	120.7
SS_0	1:3:3:5	100/202(2)	1.1/1.8	50/120	320–331	4.8	50	6.2 (0.04)/12.2(0.14)[b]	37	64.9

[a] refer to the fraction **T_0^***, residue after separation of bigger **TT_0** nanoparticles
[b] bimodal

cording to the equation [5]:

$$SAR = \frac{1}{m_{MNPs}} \cdot C \cdot \left(\frac{\partial T}{\partial t}\right)_{max} \quad (1)$$

where m_{MNPs} – is the mass of the Fe_3O_4 phase recalculated from the mass of iron in the sample determined by UV-vis spectroscopy, C – is the volume-specific heat capacity of liquid medium ($C = \rho_{hexane} \cdot c_{hexane}$; $\rho_{hexane} = 654.8\,kg/m^3$ is the density, and $c_{hexane} = 2.26\,J/g\,°C$ is the specific heat capacity of hexane), and $(\partial T/\partial t)_{max}$ is the initial slope of the heating curve. The preliminary measurements were done by adjusting magnetic field strength at $H_0 = 23.87\,kA/m$ (300 Oe) and frequency at $f = 580.5\,kHz$. For the samples $\mathbf{SS_0}$ and $\mathbf{TT_0}$ which show the best performance, the dependence of the *SAR* upon the AC magnetic field amplitude was followed for $H_0 = 3.98$, 7.96, 11.94, 15.92, 19.89 and 23.87 kA/m (or 50, 100, 150, 200, 250 and 300 Oe), at frequency $f = 580.5\,kHz$. For the sample $\mathbf{TT_0}$ additional frequency dependence of the *SAR* was followed for $f = 229.3$, 248.5, 265, 355.5, 444, 580.5 and 828 kHz, at $H_0 = 18.46\,kA/m$ (232 Oe). At least 3 measurements were done for each experimental condition (H_0, f), and an average *SAR* value is considered.

3. Results and discussion

3.1. The effect of reaction parameters on the particle size

Figs. 1 and 2 show TEM images of the as-synthesized iron oxide nanocrystals coated with nonpolar oleic acid (OA), or oleic acid and trioctylphosphine oxide (OA + TOPO). The histograms of particle size and the evolution of the reaction temperature in time are also shown in these figures. Good size dispersion inferred from the narrow particle size distribution was found for samples $\mathbf{S_0}$ (synthesized in *1*-octadecene) and $\mathbf{E_0}$ (synthesized in *1*-eicosene). The mean particle size of samples $\mathbf{S_0}$ and $\mathbf{E_0}$ were similar, *i.e.* $<d(\mathbf{S_0})>_{TEM} \sim 7.1\,nm$ and $<d(\mathbf{E_0})>_{TEM} \sim 7.5\,nm$. A bimodal particle size distribution was found for sample $\mathbf{SS_0}$ obtained by a seed-mediated procedure, and sample $\mathbf{T_0}$ synthesized in the presence of OA and TOPO molecules, where particles of size >10 nm were observed. Sample $\mathbf{T_0}$ was composed of two fractions, $\mathbf{T_0}$* (smaller NPs, Fig. 1) and $\mathbf{TT_0}$ (bigger NPs, Fig. 2). The

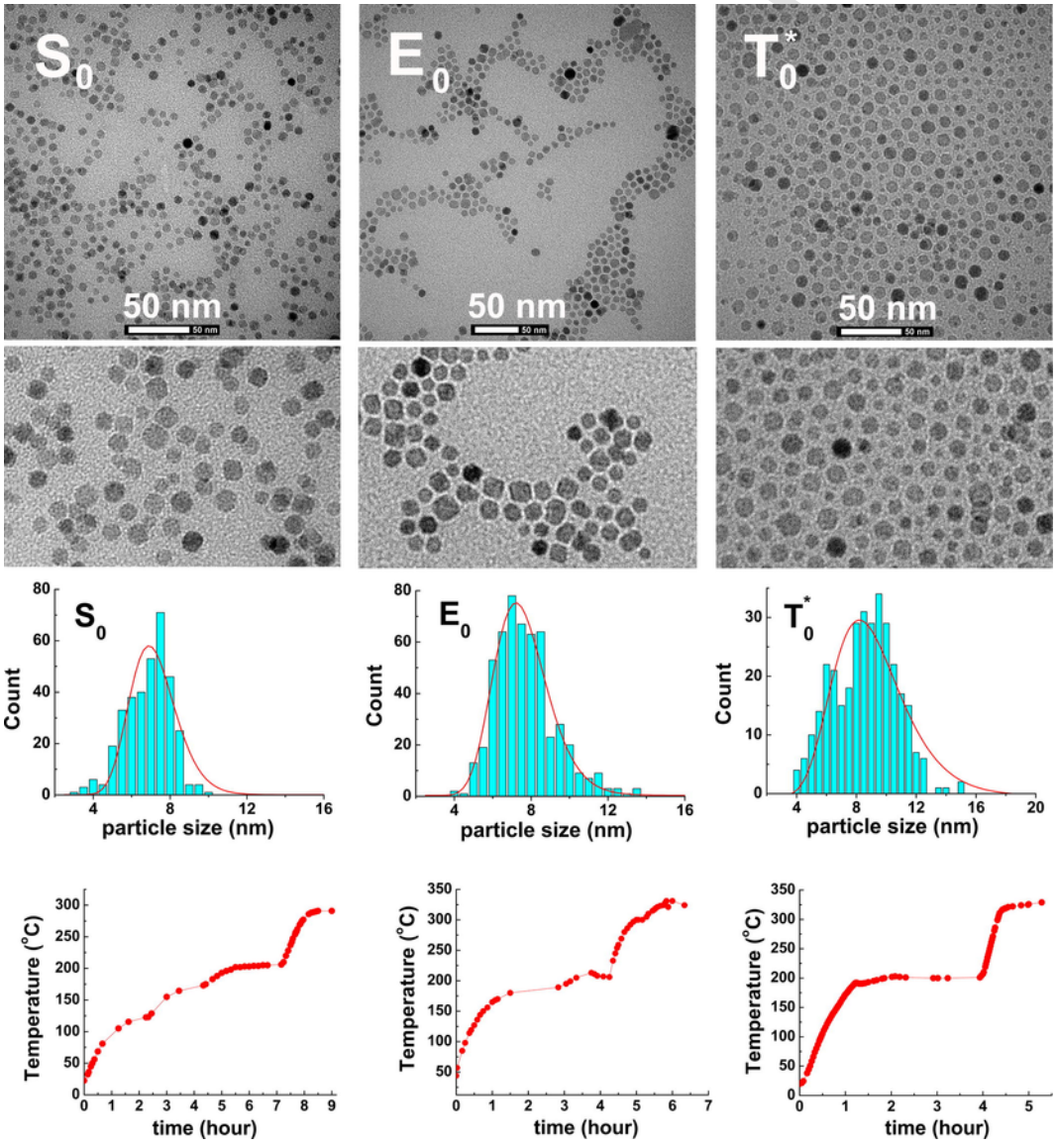

Fig. 1. TEM images of the samples $\mathbf{S_0}$, $\mathbf{E_0}$ and $\mathbf{T_0}^*$.

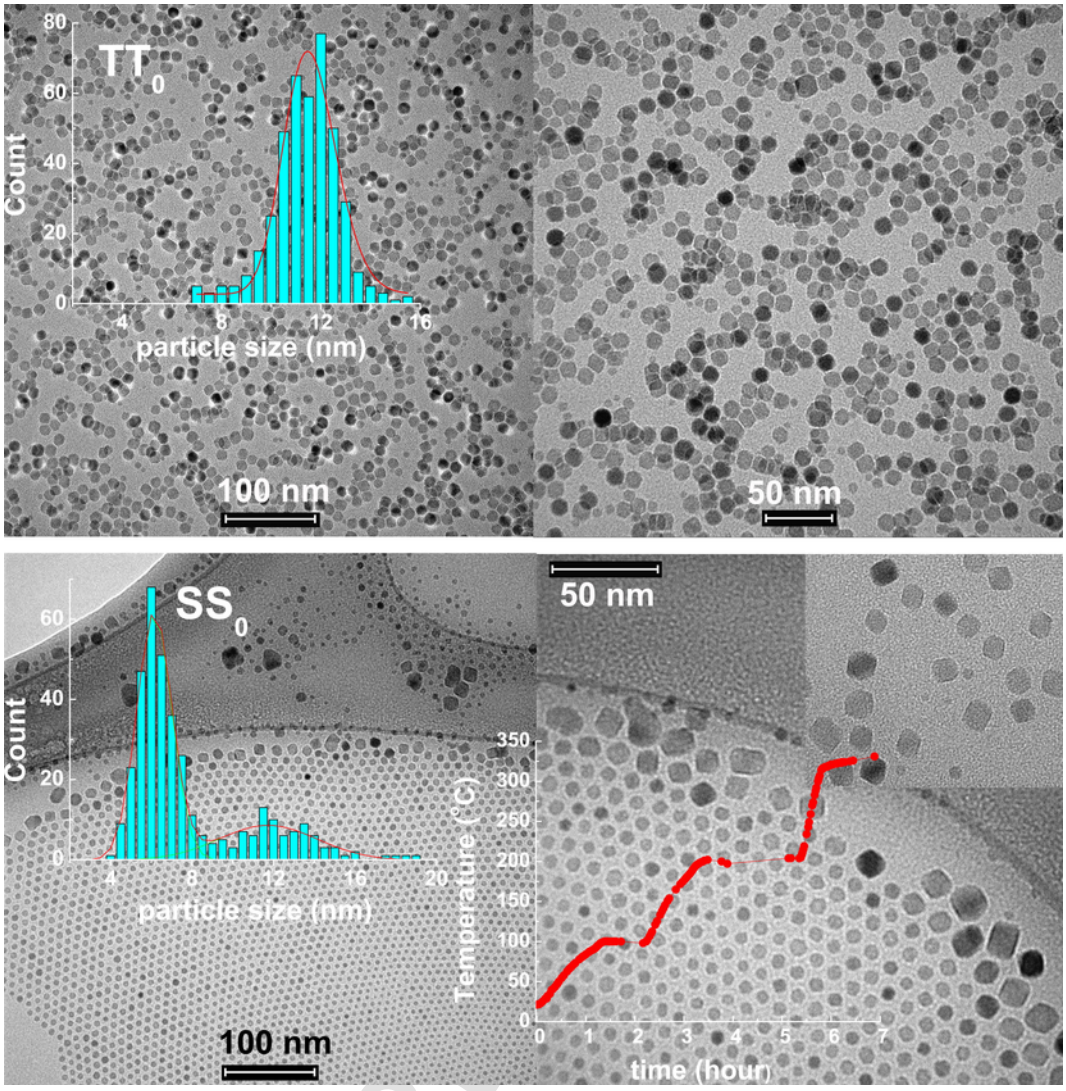

Fig. 2. TEM images of the sample $\mathbf{TT_0}$ obtained by size sorting of $\mathbf{T_0}$ nanoparticles, and the sample $\mathbf{SS_0}$ obtained by a seed-mediated procedure.

formation of self-organized $\mathbf{SS_0}$ nanoparticles at almost constant distances surrounded by bigger ones, observed during preparation of the sample for TEM (Fig. 2), indicates narrow particle size distribution and their hydrophobicity [49]. Except for the sample $\mathbf{SS_0}$, the concentration of $Fe(acac)_3$ salt in alcohol was kept constant in all reactions (0.1 mol of Fe^{3+} ions per dm^3 of solvent). Therefore, this parameter can be excluded as one which influences the particle size increase observed in the sample $\mathbf{T_0}$. Further, when the aging times, t_1 and t_2, at temperatures T_{1max} and T_{2max} respectively, and the heating rates, $\Delta T_1/\Delta t_1$ and $\Delta T_2/\Delta t_2$, were kept the same or at very similar values during the synthesis, no significant changes in the average particle size of samples $\mathbf{S_0}$ and $\mathbf{E_0}$ were found even if the final reaction temperature, T_{2max}, differs for at least 30 °C (see Table 1). But, when the heating rate to reflux, $\Delta T_2/\Delta t_2$, has been increased from ~1.7–1.9 °C/min to ~4.8 and 5.1 °C/min, as in the samples $\mathbf{SS_0}$ and $\mathbf{T_0}$ respectively, we observed a slight increase in an average size. For the sample $\mathbf{T_0}$ an initial heating rate was also higher ($\Delta T_1/\Delta t_1 \sim 3.4$ °C/min). Previous studies have shown that a heating rate to reflux may be the most important factor in determining particle size when a classical protocol in thermal decomposition of $Fe(acac)_3$ takes place [30]. Similarly, varying heating rate influences nanoparticle morphology (pyramidal, cubic and "spherical-like" octahedrons were obtained with increasing heating rate from 1.3 to 10 °C/min) [29]. H. Yang et al. revealed that higher heating rates (from 15 to 35 °C/min) favor formation of Fe_3O_4 nanocubes [28]. In any case, a heating rate to reflux should be scaled together with the concentration of iron salt in solvent in order to determine more precisely their influence on the particle size. To synthesize particles with larger average particle size, solvents with higher boiling point can be used, although it seems more effective to reduce or eliminate the amount of polyalcohol (acting as a reducing agent) [50]. This approach can be considered as a non-standard.

The classical synthesis protocol using capping ligands can also tune the final particle size and shape through the ratio of capping ligands to the concentration of iron precursor [26,28,31,33]. In our case the ratio of oleic acid (OA) and oleylamine (OM) molecules relative to Fe^{3+} ions was kept constant (3:1), except in the sample $\mathbf{S_0}$ (5:1) (see Table 1). In the samples $\mathbf{S_0}$ and $\mathbf{E_0}$, when OA and OM molecules were the only used capping ligand, insignificant or very small fraction of nanocrystals with $d > 10$ nm were observed. But, when the branched TOPO molecules were used together with OA and OM in the synthesis of $\mathbf{T_0}$ nanoparticles, a significant fraction of nanocrystals with diameter $d \sim 12$ nm was found (sample $\mathbf{TT_0}$, Fig. 2). Now, we can wonder if the presence of branched TOPO molecules could be responsible for extra crystal growth, besides the heating rate. Since the molar ratio TOPO:OA was 1:3, according to the literature it is more likely that the introduction of

TOPO during synthesis does not affect the overall size of iron oxide nanoparticles [25].

In terms of particle shape, it can be seen that the smaller nanocrystals are spherical or nearly spherical, while bigger nanocrystals have more irregular shape (Figs. 1 and 2). Oleic acid molecule has relatively large free energy of adsorption to the iron oxide surface and preference to be selectively bound onto the nanoparticle surface, while OM molecules have ability to be isotropically bound. Therefore, the oleic acid can enforce a selective face growth what can result in faceted nanoparticles. It seems that the molar ratio of oleic acid to the concentration of iron cations in all investigated samples was high enough to promote slight irregularity in the shape of nanoparticles, while the use of TOPO co-ligand could be responsible for less-faceted nanoparticles (Fig. 1) [25].

Existence of nanoparticles aggregates in the solution and their estimated average size were checked by measuring hydrodynamic diameters, d_{hyd}. No big aggregates of **S$_0$** and **SS$_0$** nanoparticles were formed in the solution, what is confirmed by the low hydrodynamic diameter, d_{hyd}(**S$_0$**)∼59 nm and d_{hyd}(**SS$_0$**)∼37 nm. On the other side, bigger aggregates exist in the samples **E$_0$**, **T$_0$*** and **TT$_0$** (see Table 1), which are usually related to strong interparticle dipole-dipole interactions. The samples **S$_0$** and **E$_0$**, with almost the same mean particle size and distribution widths, show different degree of clustering (see Table 1), probably originated in a different amount of OA molecules adsorbed on the MNPs surface, with a thicker OA-coating on the surface of **S$_0$** nanoparticles due to the synthesis conditions. The thicker coating in turn could yield to weaker interparticle interactions. The highest d_{hyd} value was found in the sample **TT$_0$**, (d_{hyd}(**TT$_0$**)∼510 nm), where magnetic interactions are expected to be the strongest due to the size and possible diminishing effect of OA shielding in the presence of TOPO molecules.

3.2. XRD analysis

The XRD patterns of iron oxide nanoparticles, synthesized by decomposition of Fe(acac)$_3$ salt in an organic phase, are shown in Fig. 3. The diffraction peaks are indexed to the spinel structure. The lattice parameter calculated from XRD patterns is ≅8.34 Å for all samples, which is close to the standard lattice parameter of maghemite (8.346 Å), rather than magnetite (8.39 Å). The position of (5 1 1) peak in all samples is at 2θ∼57.2° (57.3° for maghemite phase). In addition, the (5 1 1) peak is symmetric indicating a single oxide phase, not the mixture of magnetite and maghemite [51]. Appearance of extra peak of low intensity at 2θ∼23.63° (not shown), is observed solely in the sample **T$_0$*** and can be assigned to the (2 1 0) reflection of γ-Fe$_2$O$_3$ phase.

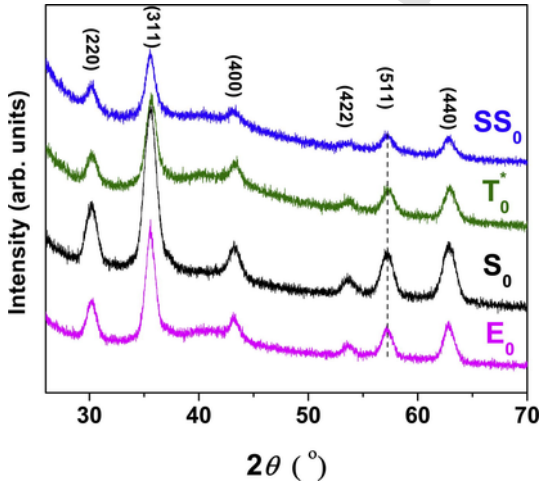

Fig. 3. X-ray diffraction patterns of the samples **S$_0$**, **E$_0$**, **T$_0$*** and **SS$_0$**.

Generally, the appearance of peaks (2 1 0) and (2 1 1) of low intensity in maghemite can be due to partial vacancy ordering at octahedral sites (S.G. $P4_132$). Since the XRD measurements were done after a few months of sample's storage, we cannot discard the possibility that the magnetite nanoparticles are transformed during the time to chemically more stable maghemite phase. The oxidation is more pronounced in the sample **T$_0$*** which in addition to OA/OM contains TOPO co-ligand. The mean crystallite size was calculated from the breadth of the (3 1 1) reflection using Scherrer's formula [52]. The obtained $<d>_{XRD}$ values are 6.6, 8, 7.1 and 7.9 nm for the samples **S$_0$**, **E$_0$**, **T$_0$*** and **SS$_0$**, respectively, indicating monodomain crystal structure. Higher difference of $|<d>_{TEM}-<d>_{XRD}|$, observed in the sample **T$_0$*** can be an indication of higher density of imperfections in the crystal structure.

3.3. Magnetic properties of oleic acid coated iron oxide nanoparticles (OA-MNPs)

The magnetic properties of as-synthesized iron oxide NPs were studied using SQUID magnetometer. Fig. 4a,b show the magnetization of OA-MNPs, **S$_0$**, **E$_0$**, **T$_0$*** and **SS$_0$**, as a function of applied field, $M(H)$, recorded at 5 and 300 K. The nanoparticles exhibit pure superparamagnetic (SPM) behavior at 300 K. Only in the sample **S$_0$** negligible the coercive field, H_C and remanent magnetization, M_R have been found at 300 K (Table 2). High saturation magnetization, M_S, shown by the samples **S$_0$**, **E$_0$** and **SS$_0$** at 300 K (M_S = 68–80.7 Am^2/kg$_{Fe3O4}$) is somewhat below the value found in the bulk magnetite (90–95 Am^2/kg) [53]. The M_S decrease degree of 18, 25 and 10% compared with the bulk counterpart, observed in the samples **S$_0$**, **E$_0$** and **SS$_0$** respectively, is proportional to spin canting contribution and density of cation vacancies inside the crystal structure. The most pronounced spin disordering has been found in the sample **T$_0$*** (Table 2). It can be due to the presence of TOPO co-ligand on the surface of **T$_0$*** nanoparticles. It was found that when the OA is prevailing surfactant molecule (as in the samples **S$_0$**, **E$_0$** and **SS$_0$**) the surface spin configuration will not differ significantly from those inside the nanoparticles core [47]. On the contrary, additional presence of branched TOPO molecule probably causes higher spin disordering at the surface. Beside the surface spin configuration, the interior magnetic ordering of the nanoparticles can differ even when the same synthesis method is used. Interior spin canting can occur in the vicinity of antiphase boundaries, dislocations, or other types of crystal imperfections. It was found that antiphase boundaries are the prevailing internal defects in iron oxide nanoparticles prepared by thermal decomposition methods [45]. At T = 5 K, low H_C and M_R values are observed in all investigated samples, while the saturation magnetization values are higher than M_S measured at 300 K (see Table 2).

The magnetization *versus* temperature curves measured under ZFC and FC conditions in a field of H_0 = 7.96 kA/m (100 Oe) are also shown in Fig. 4. The ZFC curves exhibit a maximum at T_{max}, while the bifurcation of FC and ZFC curves started at the irreversible temperature, T_{irr} (Table 2). A narrow peak in the ZFC magnetization curve of the samples **S$_0$** and **T$_0$*** at T_{max}, as well as a small difference of T_{irr}-T_{max}, reflect a very narrow size distribution. The broaden size distribution characterizes samples **E$_0$** and especially **SS$_0$** (in the sample **SS$_0$** the size distribution can be considered as bimodal) (Fig. 4c). At very low temperatures the FC magnetization curves tend to saturate, and this feature together with the observed values of remanent-to-saturation magnetization ratios, $M_R/M_S < 0.5$ at low temperature, indicate non-negligible dipolar interactions in our samples. Above T_{irr} an ensemble of magnetic nanoparticles exhibits superparamagnetic behavior (magnetic moments are unblocked, freely rotates in all directions). The blocking temperature T_B of a single domain magnetic particle is riched when the thermal energy, k_BT is comparable to the magnetic anisotropy energy, $E = K_{eff}V$,

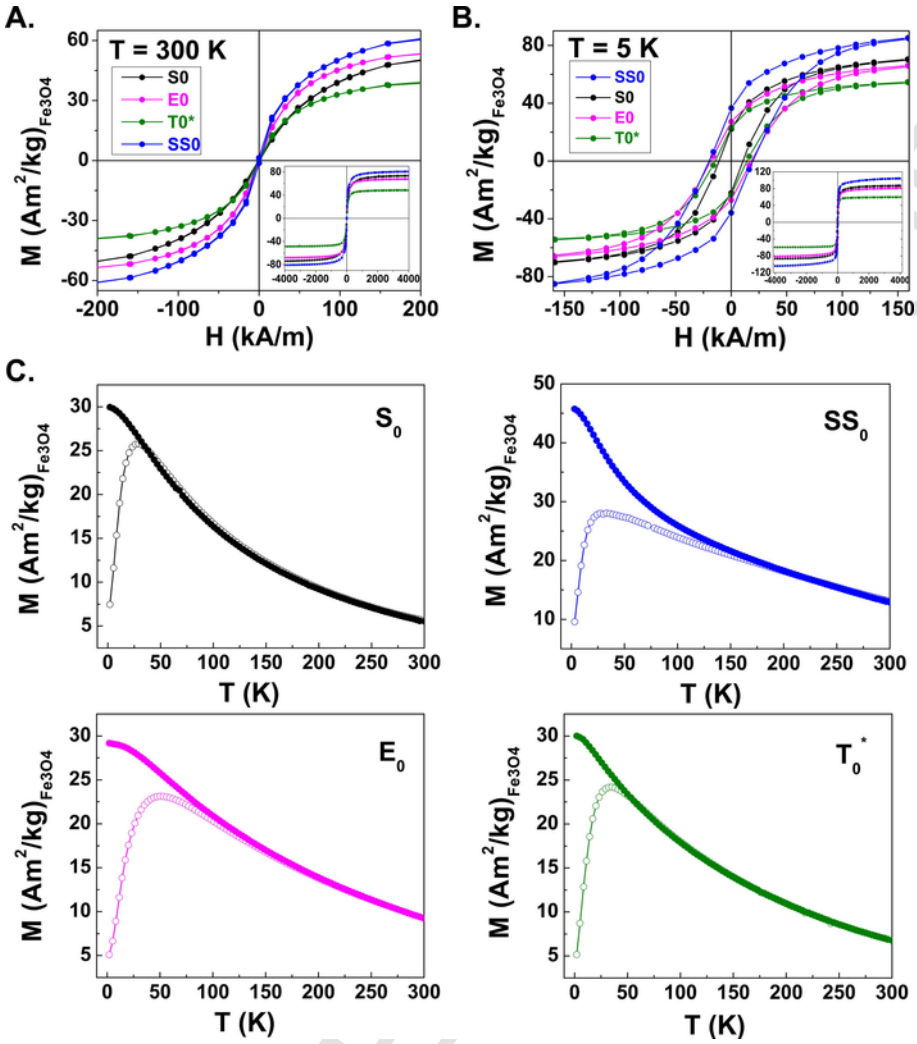

Fig. 4. Magnetization *versus* magnetic field at (a) 300 and (b) 5 K for the samples $\mathbf{S_0}$, $\mathbf{E_0}$, $\mathbf{T_0}^*$ and $\mathbf{SS_0}$ in the organic phase. (c) Zero-field-cooled (open symbol) and field-cooled (filled symbol) magnetization *vs.* temperature of iron oxide nanoparticles in a field $H_0 = 7.96$ kA/m (100 Oe).

Table 2
Remanent magnetization ($\boldsymbol{M_R}$), saturation magnetization ($\boldsymbol{M_S}$), ratio $\boldsymbol{M_R/M_S}$ and coercitive field ($\boldsymbol{H_C}$) estimated from the hysteresis loops measured at 5 and 300 K; the position of the maximum of ZFC magnetization ($\mathbf{T_{max}}$), irreversible temperature ($\mathbf{T_{irr}}$), estimated average blocking temperature ($\langle \mathbf{T_B} \rangle$), parameter $\boldsymbol{\kappa} = \mathbf{T_{max}}/\langle \mathbf{T_B} \rangle$, and effective anisotropy constant ($\boldsymbol{K_{eff}}$)*.

Sample	T [K]	M_R [Am²/kg]	M_S [Am²/kg]	M_R/M_S at 5 K	H_C [kA/m]	T_{max} [K]	T_{irr} [K]	$\langle T_B \rangle$ [K]	κ	K_{eff}* [kJ/m³]
S_0	5	22.3	87.1	0.26	10.8	28	33	15	1.87	27.6
	300	6	73.6	–	1.1					
E_0	5	27	81.4	0.33	18.2	48	117	26	1.84	40.6
	300	0	68	–	0					
T_0^*	5	22.8	59.9	0.38	14.2	31	43	17.8	1.74	17.2
	300	0	48.4	–	0					
SS_0	5	36.1	104.4	0.34	19.7	57	168	14.6	3.9	–
	300	0	80.7	–	0					

* $K_{eff} = 25 k_B \langle T_B \rangle / V_{TEM}$; $\langle T_B \rangle$ was estimated as a maximum of $\partial(T \cdot M_{ZFC})/\partial T$.

(where K_{eff} – is the effective magnetic anisotropy, k_B – is the Boltzmann's constant and V – is the particle volume).

For a real system, composed of a dispersion of particles, broadening of the ZFC magnetization curves, $M_{ZFC}(T)$, reflects the width of the size distribution, which results in a distribution of blocking temperatures, $f(T_B)$. Assuming that $f(T_B) \sim \partial(TM_{ZFC})/\partial T$, we estimated the most probable blocking temperature $\langle T_B \rangle$ for an ensemble of nanoparticles as a maximum in the first derivative of $TM_{ZFC}(T)$ product with respect to temperature [54]. This value, related to a mean diameter $\langle d \rangle$, was used to calculate the effective anisotropy constant, K_{eff}, by the use of $25 k_B \langle T_B \rangle = K_{eff} V$ relation, valid for noninteracting nanoparticles and low values of applied magnetic field (i.e., below the anisotropy field of the material). Volume of nearly spherical NPs has been calculated as $V = \pi \langle d \rangle^3 / 6$. The estimated $\langle T_B \rangle$ and K_{eff} values are given in Table 2. It can be notice that the samples $\mathbf{S_0}$ and $\mathbf{SS_0}$ have very similar mean blocking temperature, $\langle T_B \rangle$ (see Table 2); $\mathbf{SS_0}$ is obtained by a seediated

process starting from $\mathbf{S_0}$ as seeds. However, since the sample $\mathbf{SS_0}$ is characterized by a bimodal size distribution, $K_{eff}(\mathbf{SS_0})$ has not been estimated due to the impossibility of relating $\langle T_B \rangle$ to $\langle d \rangle$. For the samples $\mathbf{S_0}$ and $\mathbf{E_0}$, coated with OA, we take that the magnetic core of the nanoparticles coincides with the diameter of particle determined from TEM observation [47], while for the sample $\mathbf{T_0}^*$ (coated with TOPO co-ligand) such assumption can be questionable since the spin disordering is the most pronounced in this sample (see Table 2). If we consider that in the sample $\mathbf{T_0}^*$, $\langle d \rangle = \langle d_M \rangle$, where $\langle d_M \rangle$ – is the average magnetic particle diameter estimated taking Chantrell's equation [55,56]:

$$\langle d_M \rangle = \left[\frac{18 k_B T}{\pi M_s \rho} \sqrt{\frac{\chi_i}{3 m_s H_0^{ex}}} \right]^{1/3} \quad (2)$$

then we obtain $\langle d_M \rangle \cong 7.5$ nm, and consequently $K_{eff} \cong 27.8$ kJ/m^3, which is in good agreement with the value $K_{eff}(\mathbf{S_0})$ (see Table 2). On the contrary, if we take $\langle d \rangle = \langle d \rangle_{TEM}$, $K_{eff}(\mathbf{T_0}^*)$ has lower value given in Table 2. Lower anisotropy in the sample $\mathbf{T_0}^*$ could be due to a partial oxidation of magnetite to maghemite phase facilitated by the presence of TOPO molecules at the surface ($K_V(\gamma\text{-}Fe_2O_3) = 4.5$ kJ/m^3) [7]. High anisotropy was found in the sample $\mathbf{E_0}$ ($K_{eff}(\mathbf{E_0}) = 40.6$ kJ/m^3). Anyway, the estimated K_{eff} values of our samples are in the range reported in the literature for magnetite nanoparticles (10–41 kJ/m^3) [4,7]. The increase of K_{eff} values relative to the magnetocrystalline anisotropy of magnetite ($K_V(Fe_3O_4) = 11$–14 kJ/m^3) [7] usually is attributed to the surface and strain anisotropy contribution, although the anisotropy due to particle's magnetic interactions cannot be excluded.

As we can see, the increase in K_{eff} value is more prominent in the sample $\mathbf{E_0}$. Also, in this sample the T_{irr} and $\langle T_B \rangle$ values are higher than in the samples $\mathbf{S_0}$ and $\mathbf{T_0}^*$. In addition, the coercitive filed, H_C of $\mathbf{E_0}$ is higher comparing with H_C of $\mathbf{S_0}$ irrespective of the similar mean particle size (see Table 2). Since the volumes of $\mathbf{S_0}$ and $\mathbf{E_0}$ NPs are very similar, the experimentally observed increase in H_C of $\mathbf{E_0}$ probably comes from higher anisotropy constant, K_{eff} and slightly lower saturation magnetization, M_S of $\mathbf{E_0}$ [57]. All these facts point out that the magnetostructural features of the sample $\mathbf{E_0}$ synthesized in *1*-eicosene differ comparing to the samples synthesized in *1*-octadecene.

In addition, we can notice that the maximum in the ZFC curve at T_{max} is shifted relative to the most likely blocking temperature value $\langle T_B \rangle$ for a factor $\kappa = 1.87$, 1.84 and 1.74 ($T_{max} = \kappa \langle T_B \rangle$) in the samples $\mathbf{S_0}$, $\mathbf{E_0}$ and $\mathbf{T_0}^*$, respectively, while in the sample $\mathbf{SS_0}$ $\kappa = 3.9$. κ values theoretically estimated for a system of small magnetic particles with a narrow and log-normal volume distribution, and K_{eff} fixed at 32 kJ/mol, lie in the range 1–2 [58]. Higher κ value observed in the sample $\mathbf{SS_0}$ results from a wider and bimodal size distribution.

3.4. Power absorption of OA-MNPs

The above described magnetization behavior of the samples has been studied in a static regime. Further characterization was performed through the heating ability of OA-MNPs in the organic medium (hexane) when they are subjected to an oscillating external field. Different heating mechanisms can take place simultaneously [7,12,43]. In order to determine the dominant one under given conditions (H_0,f), it is important to determine the regime which controls magnetic behavior of an ensemble of nanoparticles during the experimental time window, $\tau_{meas} = 1/2\pi f$. In an oscillating external field system of magnetic nanoparticles can be in a state close to equilibrium (i.e. superparamagnetic), or in a metastable state. Among various parameters, the main parameter which controls the type of behavior is the ratio H_0/H_K, where $\mu_0 H_K = 2K_{eff}/\rho M_S$ is the anisotropy field of the material [8]. If $H_0/H_K << 1$, the system is in a SPM regime. If $H_0/H_K > 1$, metastable behavior is favoured [8]. Since H_K depends on magnetic anisotropy constant, K_{eff}, this parameter can be considered as a crucial one in determining the dominant mechanism of heating. As we already mention, many experimental and theoretical results have shown that the best heating ability will achieve those nanoparticles with size just above the transition from SPM to ferromagnetic regime [12]. In our case, for an ensemble of NPs with the lowest estimated magnetic anisotropy ($K_{eff} \cong 18$ kJ/m^3) and the highest saturation magnetization (~81 Am^2/kg, i.e. ~420 kA/m) at room temperature, the minimum value of H_K is ~68 kA/m, while the maximum applied field amplitude in the experiments was $H_0 = 23.87$ kA/m. Thus, we can consider that for applied experimental conditions our systems were in the SPM regime, and that the power losses in an AC magnetic field were generated solely by the relaxation processes (Néel and Brownian).

In Table 1 are summarized the *SAR* values of OA-coated nanoparticles obtained under experimental condition ($H_0 = 23.87$ kA/m (300 Oe), $f = 580.5$ kHz). The best heating ability show samples $\mathbf{SS_0}$, $\mathbf{T_0}^*$ and $\mathbf{TT_0}$. The samples $\mathbf{E_0}$ and $\mathbf{S_0}$ with similar mean particle size around 7 nm do not heat significantly, what is expected, since the iron oxide NPs with a mid-range K_{eff} value (~25 kJ/m^3) and size smaller than about 7 nm do not participate in the heat dissipation in a low-viscosity medium [7]. The slight increase of the *SAR* of the sample $\mathbf{E_0}$, compared to the sample $\mathbf{S_0}$, can be assigned to the contribution of bigger particles with $d > 10$ nm (see the particle size distribution, Fig. 1). Special attention has been paid to the sample $\mathbf{TT_0}$ with $<d>_{TEM} \sim 11.6$ nm. It was revealed that nanoparticles about 12 nm in size can be the most promising hyperthermia mediators since their heating ability is not influenced by the media viscosity [43], which is important for biomedical applications.

For the samples $\mathbf{SS_0}$ and $\mathbf{TT_0}$ we determined the *SAR* as a function of the AC magnetic field amplitude, H_0, in the range from 3.98 to 23.87 kA/m, while it oscillated at the fixed frequency $f = 580.5$ kHz (Fig. 5a). We have found that for $H_0 > 7.96$ kA/m (100 Oe), the sample $\mathbf{TT_0}$ provides higher losses relative to the sample $\mathbf{SS_0}$ which is mainly attributed to the size effect. A quadratic dependence of the *SAR* upon field amplitude has been found in the sample $\mathbf{TT_0}$ up to $H_0 = 23.87$ kA/m (300 Oe), and in the sample $\mathbf{SS_0}$ up to $H_0 = 15.91$ kA/m (200 Oe) (Fig. 5a). At higher H_0, a decrease from the expected square law was noticed in the sample $\mathbf{SS_0}$. The tendency that *SAR* saturates at higher H_0 could be explained by lowering the energy barrier due to the Zeeman energy, or might be considered as a consequence of a diamagnetic contribution coming from the glass holder when it is sited in the AC magnetic field of higher amplitude [19,35,37]. We could also say that the *SAR* is linearly dependent on H_0 in the range from 7.96 kA/m (100 Oe) to 23.87 kA/m (300 Oe), as is shown for the sample $\mathbf{SS_0}$ (blue dashed line in Fig. 5a), but these linear curves do not intercept the origin (0,0) (no heating in the absence of the AC magnetic field). The quadratic dependence of the *SAR* value upon the magnetic field amplitude, H_0 is predicted by the linear theory for noninteracting superparamagnetic nanoparticles [4]. The linear, rather than quadratic dependence upon H_0 can be observed in a system of interacting 3dim-nanoparticle clusters [40].

As dipole-dipole interactions can influence the *SAR* values, the sample concentration is a relevant factor to be considered. In both samples the mass concentration m, of Fe_3O_4 phase in an organic medium was similar ($m_{Fe3O4}(\mathbf{SS_0}) = 9.03$ mg/ml, and $m_{Fe3O4}(\mathbf{TT_0}) = 9.485$ mg/ml), but because of different particle size the number of $\mathbf{SS_0}$ nanoparticles per volume unit of suspension has been about six times higher than the number of $\mathbf{TT_0}$ nanoparticles. In the case of homogeneous particles distribution inside the ferrofluid it implies the difference in an average interparticle's distance, $<l>$. Taking into account that $<l> \sim \rho^{1/3}.m^{-1/3}.<d>_{TEM}$, where ρ is the density of magnetite phase

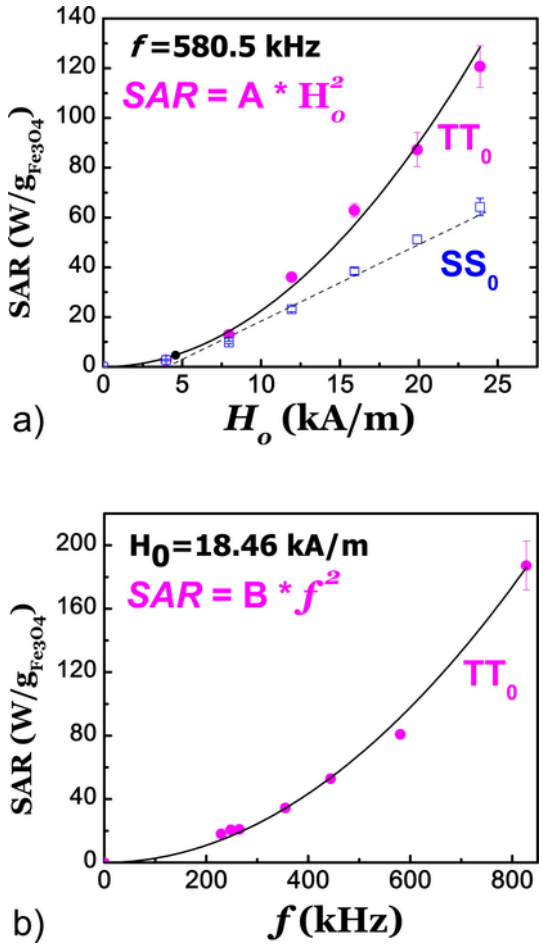

Fig. 5. a) *SAR* of the samples $\mathbf{SS_0}$ and $\mathbf{TT_0}$ *versus* AC magnetic field amplitude, H_0, measured at the frequency $f = 580.5$ kHz; b) *SAR* of the sample $\mathbf{TT_0}$ *versus* frequency, f, measured at the field amplitude $H_0 = 18.46$ kA/m. Full lines represent fitted experimental results by the quadratic function ($y = Ax^2$), while the dashed line is a guidance for eyes.

($\rho(Fe_3O_4) = 5200\,kg/m^3$), we have estimated $<l>$ of $\mathbf{TT_0}$ NPs to be ~76 nm and $<l>$ of $\mathbf{SS_0}$ NPs ~42 nm. It was revealed that the interparticle dipole-dipole interactions can be neglected for 12 nm-sized iron oxide NPs if their mutual distance is ~27 nm [10]. On the other hand, formation of aggregates at high particle concentrations can change the heating ability of ferrofluids involving collective particles behavior as essential factor in determining *SAR* [7,11,38,48,59]. For oleic acid capped iron oxide nanoparticles, magnetic dipolar interactions are responsible for aggregation. Another question can come into play regarding the possibility that the configuration of loosely bonded aggregates can be changed under exposing to AC magnetic field [60]. Measurements of the hydrodynamic diameter of the samples $\mathbf{SS_0}$ and $\mathbf{TT_0}$ implies formation of significantly larger aggregates in the sample $\mathbf{TT_0}$ compared to the sample $\mathbf{SS_0}$ (see Table 1), which can be expected since the magnetic moment of one $\mathbf{TT_0}$ nanoparticle is higher than the magnetic moment of $\mathbf{SS_0}$ nanoparticle.

In the sample $\mathbf{TT_0}$ with the best size and shape homogeneity of the nanocrystals, additional frequency dependence of the *SAR* value has been studied in the frequency range (229.3–828) kHz at fixed AC field amplitude $H_0 = 18.46$ kA/m (232 Oe). We have found that the f dependence do not follow a linear, but a quadratic increase within the whole investigated range (Fig. 5b). The linear dependence of the *SAR vs.* f can be considered for frequencies up to $f \sim 600$ kHz, but again such linear curve does not intercept the origin (0,0). We should notice that the experiment was performed for H_0 value for which the $SAR \sim H_0^2$, allowing us to work under the validity of linear response theory (LRT), neglecting eventual presence of interparticle dipolar interactions. The LRT theory predicts that the heat dissipation of superparamagnetic fluids will depend on frequency via a square law in the low frequency range when $2\pi f\tau_R << 1$, where $\tau_R = (\tau_N \cdot \tau_B)/(\tau_N + \tau_B)$, and τ_N and τ_B are the characteristic time of the Néel and Brownian relaxations process, respectively [2,7,10,43].

In order to check the critical frequency for the system of $\mathbf{TT_0}$ NPs, we considered our system to be a concentrated one (with aggregates of nanoparticles), as well as a system with bidispersed structures (composed of stable nanoclusters and well-dispersed NPs). The Néel and Brownian relaxation times, τ_N and τ_B, have been calculated for NPs with different size: 7, 10, 11.6 and 13 nm. The characteristic time of the Néel relaxations process, $\tau_N = \tau_0 \exp[K_{eff}V/k_BT]$, for NPs with selected size and $K_{eff} = 18$, 25, 33 or 40 kJ/m^{3}values, has been found to be in the range from nano- to microseconds (Table 3). For $<K_{eff}>$ values have been taken those which cover the range of estimated magnetic anisotropy constant in our systems (under assumption that NPs do not interact and that the ratio H_0/H_K is $<< 1$). For the attempt time, τ_0, the value 10^{-9} s was taken, valid for superparamagnetic nanoparticles, and T = 300 K. Considering the ferrofluid $\mathbf{TT_0}$ as a concentrated system, the Brownian relaxation time, τ_B^{hyd}, was obtained to be of the order of millisecond ($\tau_B^{hyd}(\mathbf{TT_0})_{510nm} = 4\pi\eta r_{hyd}^3/k_BT = 14.9$ ms; η – is the dynamic viscosity of the solution; $\eta_{hexane} = 294.9\times10^{-6}$ kg/s·m at room temperature). On the contrary, the Brownian relaxation time for independent NPs, τ_B^{indep}, assuming additional increasing of d for 4 nm (the lenght of oleic acid molecule is ~2 nm), has been found to be around 150, 309, 427 and 553 ns for 7, 10, 11.6 and 13 nm sized NPs, respectively. It is well known that the prevailing mechanism in heat dissipation will be the one with lower relaxation time. Hence, in a concentrated system, the heating coming from the Brownian relaxation of the aggregated NPs is insignificant and the Néel mechanism dominates. The situation can be changed significantly only for bigger NPs (>12 nm), if they are well-dispersed (nonaggregated). In that case the Brownian relaxation modifies the relaxation time τ_R and shift condition $\omega\tau_R < 1$ to mid-range anisotropy values (~25 kJ/m^3).

Based on the above analysis we can assume that the Néel relaxation is the main process by which magnetic energy is absorbed in $\mathbf{TT_0}$ sample. Then, for NPs with size up to 10 nm, $\omega\tau_N << 1$ in the whole exper-

Table 3
Calculated Néel relaxation time, $\tau_N = \tau_0 \exp[K_{eff}V/k_BT]$, and the product $2\pi f\tau_N$ in the experimentally determined frequency range of applied AC magnetic field from 229.3 to 828 kHz, for nanoparticles with selected size, $<d>$, and effective anisotropy constant, K_{eff}. Value of τ_0 was taken to be 10^{-9} s, T = 300 K and $V = \pi\langle d\rangle^3/6$.

$<d>$ (nm)	7		10		11.6		13	
K_{eff} (kJ/m^3)	τ_N (ns)	$2\pi f\tau_N$	τ_N (ns)	$2\pi f\tau_N$	τ_N (ns)	$2\pi f\tau_N$	τ_N (ns)	$2\pi f\tau_N$
18	1.28	0.002–0.007	9.7	0.01–0.05	35	0.05–0.18	148	0.21–0.77
25	1.41	0.002–0.007	23.6	0.03–0.12	139	0.20–0.72	1036	1.49–5.4
33	1.58	0.002–0.008	64.8	0.09–0.34	672	0.97–3.5	9557	13.8–50
40	1.74	0.002–0.009	157.0	0.23–0.82	2678	3.8–13.9	66776	>>1

imental *f*-range (229.3–828 kHz), regardless of K_{eff} value (see Table 3). For NPs with size 11.6 nm the condition $\omega\tau_N << 1$ is satisfied up to $K_{eff} \approx 25\,kJ/m^3$, while with further increase of the magnetic anisotropy constant the product $\omega\tau_N$ approaches to one, firstly at high frequency. In the highly anisotropic system of ~12 nm sized NPs (when $K_{eff} > 33\,kJ/m^3$), $\omega\tau_N > 1$, and the system is in a blocked state. The experimentally observed quadratic *SAR* dependence on frequency in the system of $\mathbf{TT_0}$ NPs, coincidences with theoretical prediction if we suppose that $\mathbf{TT_0}$ NPs have lower magnetic anisotropy (no more than $\sim 25\,kJ/m^3$). From the magnetic measurements we estimated the value $K_{eff} = 17.8\,kJ/m^3$ for the system of $\mathbf{T_0}^*$ NPs. It is reasonable to believe that both samples, $\mathbf{T_0}^*$ and $\mathbf{TT_0}$, have lower K_{eff} since they are coated with TOPO co-ligand which can provoke a partial oxidation of magnetite phase. In the literature, the nearly quadratic *f*-dependence of the *SAR* has been found in NPs around 8 nm in size, but not in the systems of bigger NPs with an average size around 11 and 13 nm [43]. The measurements were performed under conditions ($H_0 = 4\,kA/m$, $f = 166–739.2\,kHz$), at concentration of 50 mg_{Fe}/ml, and the systems have been characterized as magnetically highly anisotropic ($K_{eff} \sim 67\,kJ/m^3$) [43]. In this work we have shown that the ensemble of ~12 nm NPs at concentration of ~9.4 mg_{Fe3O4}/ml and with $K_{eff} < 25\,kJ/m^3$, can follow the quadratic *f*-dependence of the *SAR* in the AC magnetic field up to $f = 828\,kHz$. System will be in a non-equilibrium, metastable state when characteristic relaxation time, τ_R becomes much larger than $\tau_{meas} = 1/2\pi f$, and then the hysteretic process comes into play. In our case, it is possible only for 14 nm NPs when they are subjected to high frequency AC magnetic field of $f = 828\,kHz$ (then, $\tau_{meas} = 192\,ns < \tau_R^{min} = 288\,ns$). Since their number is insignificant compared to those with 12 and 13 nm (see Fig. 2), we have neglected the contribution of conventional hysteresis losses in the process of magnetic energy dissipation and we declare that our system dissipate power exclusively through the Néel relaxation processes.

It is obvious, that, in order to be more precise in defining the critical/optimal size for magnetic hyperthermia, we should additionally pay attention to the K_{eff} value, as well as to the size and magnetic anisotropy distributions. It was revealed that the optimal diameter of NPs for use in hyperthermia lies between 12 and 20 nm [7]. In our case, the maximum *SAR* value of the sample $\mathbf{TT_0}$ measured under conditions ($H_0 = 18.46\,kA/m$, $f = 828\,kHz$) was $187.2\,W/g_{Fe3O4}$. For 13 nm NPs the measured *SAR* under ($H_0 = 20\,kA/m$, $f = 765\,kHz$) has been reported to be as high as ~100 W/g [12], while the *SAR* of 16 nm maghemite cubes was 1650 $W/g_{\gamma\text{-}Fe2O3}$ under ($H_0 = 18.46\,kA/m$, $f = 700\,kHz$) [61]. The optimal diameter of NPs for effective heating under given experimental conditions is influenced by the magnetostructural features of materials (size, shape, NPs coating, magnetic anisotropy, magnetic saturation value, size distribution, degree of NPs aggregation, inter- and intraparticle interactions between the aggregates). Therefore, when some system is examined for hyperthermia, it is very important to analyze each of these aspects as much as possible.

4. Conclusions

In this work, iron oxide nanocrystals were synthesized by thermal decomposition method of $Fe(acac)_3$ in the presence of surfactants and a reducing agent. Keeping the concentration of iron ions in solvent constant (1 mol of Fe^{3+} in 80 ml of solvent), we found that a heating rate to reflux can be the most important factor in determining the particle size. Nearly all nanoparticles showed spherical shape with slight deviations, the pronounced faceted morphology being observed in sample synthesized with *1*-eicosene. Spin disordering and phase instability was found in the sample coated with TOPO co-ligand in coexistence with oleic acid and oleyamine. The relatively low anisotropy constants found in our samples, i.e., $K_{eff} = 17–41\,kJ/m^3$, make our systems suitable as heating agents under *in vivo* conditions. The main contribution to the sample heating coming from the Néel relaxation process could be quantitatively modeled with further control on the degree of nanoparticles aggregation under *in vitro* conditions.

Acknowledgements

This work was supported by the Ministry of Education, Science and Technological Development (MESTD) of the Republic of Serbia through the project No. 45015. N.J.O. would like to thank MESTD for the postdoctoral fellowship at the Institute of Nanoscience of Aragon, University of Zaragoza, Spain, and Prof. Goya for kind hospitality in his laboratory. G.F.G. and M.P.C. thank financial support from the DGA (Gobierno de Aragon, Project E26) and Spanish Ministerio de Economia y Competitividad (MINECO) through project MAT2013-42551.

Appendix A. Supplementary data

Supplementary data associated with this article can be found, in the online version, at https://doi.org/10.1016/j.jmmm.2017.10.053.

References

[1] R. Hergt, S. Dutz, R. Müller, M. Zeisberger, Magnetic particle hyperthermia: nanoparticle magnetism and materials development for cancer therapy, J. Phys. Condens. Matter 18 (2006) S2919–S2934.
[2] R. Hergt, S. Dutz, Magnetic particle hyperthermia – biophysical limitations of a visionary tumour therapy, J. Magn. Magn. Mater. 311 (2007) 187–192.
[3] C. Xu, S. Sun, New forms of superparamagnetic nanoparticles for biomedical applications, Adv. Drug Delivery Rev. 65 (2013) 732–743.
[4] R.E. Rosensweig, Heating magnetic fluid with alternating magnetic field, J. Magn. Magn. Mater. 252 (2002) 370–374.
[5] R.R. Shah, A.R. Dombrowsky, A.L. Paulson, M.P. Johnson, D.E. Nikles, C.S. Brazel, Determining iron oxide nanoparticle heating efficiency and elucidating local nanoparticle temperature for application in agarose gel-based tumor model, Mater. Sci. Eng. C 68 (2016) 18–29.
[6] C. Blanco-Andujar, D. Ortega, P. Southern, S.A. Nesbitt, N.T.K. Thanh, Q.A. Pankhurst, Real-time tracking of delayed-onset cellular apoptosis induced by intracellular magnetic hyperthermia, Nanomedicine (Lond.) 11 (2016) 121–136.
[7] A.E. Deatsch, B.A. Evans, Heating Efficiency in Magnetic Nanoparticle Hyperthermia, J. Magn. Magn. Mater. 354 (2014) 163–172.
[8] S. Ruta, R. Chantrell, O. Hovorka, Unified model of hyperthermia via hysteresis heating in systems of interacting magnetic nanoparticles, Sci. Rep. 5 (2015) 9090.
[9] G.F. Goya, E. Lima Jr., A.D. Arelaro, T. Torres, H.R. Rechenberg, L. Rossi, C. Marquina, M. Ricardo, Ibarra, magnetic hyperthermia with Fe_3O_4 nanoparticles: the influence of particle size on energy absorption, IEEE Trans. Magn. 44 (2008) 4444–4447.
[10] H. Mamiya, Recent advances in understanding magnetic nanoparticles in AC magnetic fields and optimal design for targeted hyperthermia, J. Nanomater., 2013, ID752973.
[11] J.G. Ovejero, D. Cabrera, J. Carrey, T. Valdivielso, G. Salasabe, F.J. Teran, Effects of inter- and intra-aggregate magnetic dipolar interactions on the magnetic heating efficiency of iron oxide nanoparticles, Phys. Chem. Chem. Phys. 18 (2016) 10954–10963.
[12] K.D. Bakoglidis, K. Simeonidis, D. Sakellari, G. Stefanou, M. Angelakeris, Size-dependent mechanisms in AC magnetic hyperthermia response of iron-oxide nanoparticles, IEEE Trans. Magn. 48 (2012) 1320–1323.
[13] A.H. Lu, E.L. Salabas, F. Schulth, Magnetic nanoparticles: synthesis, protection, functionalization, and application, Angew. Chem. Int. Ed. Engl. 46 (2007) 1222–1244.
[14] M. Lévy, C. Wilhelm, M. Devaud, P. Levitz, F. Gazeau, How cellular processing of superparamagnetic nanoparticles affects their magnetic behavior and NMR relaxivity, Contrast Media Mol. Imaging 7 (2012) 373–383.
[15] D. Serantes, K. Simeonidis, M. Angelakeris, O. Chubykalo-Fesenko, M. Marciello, M. del Puerto Morales, D. Baldomir, C. Martinez-Boubeta, Multiplying magnetic hyperthermia response by nanoparticle assembling, J. Phys. Chem. C 118 (2014) 5927–5934.
[16] S.F. Hasany, N.H. Abdurahman, A.R. Sunarti, R. Jose, Magnetic iron oxide nanoparticles: chemical synthesis and applications review, Curr. Nanosci. 9 (2013) 561–575.
[17] P. Guardia, R. Di Corato, L. Lartigue, C. Wilhelm, A. Espinosa, M. Garcia-Hernandez, F. Gazeau, L. Manna, T. Pellegrino, Water – soluble iron oxide nanocubes with high values of specific absorption rate for cancer cell hyperthermia treatment, ACS Nano 6 (2012) 3080–3091.
[18] D. Ho, X. Sun, S. Sun, Monodisperse magnetic nanoparticles for theranostic applications, Accounts Chem. Res. 44 (2011) 875–882.
[19] E. Natividad, M. Castro, G. Goglio, I. Andreu, R. Epherre, E. Duguet, A. Mediano, New insights into the heating mechanisms and self-regulating abilities of mangan-

ite perovskite nanoparticles suitable for magnetic fluid hyperthermia, Nanoscale 4 (2012) 3954–3962.
[20] J.-H. Lee, J.-T. Jang, J.-S. Choi, S.H. Moon, S.-H. Noh, J.-W. Kim, J.-G. Kim, I.-S. Kim, K.I. Park, J. Cheon, Exchange-coupled magnetic nanoparticles for efficient heat induction, Nat. Nanotechnol. 6 (2011) 418–422.
[21] G.C. Lavorato, D. Peddis, E. Lima Jr., H.E. Troiani, E. Agostinelli, D. Fiorani, R.D. Zysler, E.L. Winkler, Magnetic interactions and energy barrier enhancement in core/shell bimagnetic nanoparticles, J. Phys. Chem. C 119 (2015) 15755–15762.
[22] L.-M. Lacroix, R. Bel Malaki, J. Carrey, S. Lachaize, M. Respaud, G.F. Goya, B. Chaudret, Magnetic hyperthermia in single-domain monodisperse feco nanoparticles: evidence for stoner-wohlfarth behavior and large losses, J. Appl. Phys. 105 (2009) 023911.
[23] J. Alonso, H. Khurshid, V. Sankar, Z. Nemati, M.H. Phan, E. Garayo, J.A. García, H. Srikanth, FeCo nanowires with enhanced heating powers and controllable dimensions for magnetic hyperthermia, J. Appl. Phys. 117 (2015) 17D113.
[24] E.A. Périgo, G. Hemery, O. Sandre, D. Ortega, E. Garaio, F. Plazaola, F.J. Teran, Fundamentals and advances in magnetic hyperthermia, Appl. Phys. Rev. 2 (2015) 041302.
[25] Y. Bao, T. Wen, A.C.S. Samia, A. Khandhar, K.M. Krishnan, Magnetic nanoparticles: material engineering and emerging applications in lithography and biomedicine, J. Mater. Sci. 51 (2016) 513–553.
[26] G. Gao, X. Liu, R. Shi, K. Zhou, Y. Shi, R. Ma, E. Takayama-Muromachi, G. Qiu, Shape-controlled synthesis and magnetic properties of monodisperse Fe_3O_4 nanocubes, Cryst. Growth. Design. 10 (2010) 2888–2894.
[27] S. Sun, H. Zeng, Size-controlled synthesis of magnetite nanoparticles, J. Am. Chem. Soc. 124 (2002) 8204–8205.
[28] H. Yang, T. Ogawa, D. Hasegawa, M. Takahashi, Synthesis and magnetic properties of monodisperse magnetite nanocubes, J. Appl. Phys. 103 (2008) 07D526.
[29] L. Zhang, Q. Li, S. Liu, M. Ang, M.O. Tade, H.-C. Gu, Synthesis of pyramidal, cubical and truncated octahedral magnetite nanocrystals by controlling reaction heating rate, Adv. Powder Technol. 22 (2011) 532–536.
[30] N. Miguel-Sancho, O. Bomati-Miguel, A.G. Roca, G. Martinez, M. Arruebo, J. Santamaría, Synthesis of magnetic nanocrystals by thermal decomposition in glycol media: effect of process variables and mechanistic study, Ind. Eng. Chem. Res. 51 (2012) 8348–8357.
[31] T. Kikuchi, R. Kasuya, S. Endo, A. Nakamura, T. Takai, N. Metzler-Nolte, K. Tohji, J. Balachandran, Preparation of magnetite aqueous dispersion for magnetic fluid hyperthermia, J. Magn. Magn. Mater. 323 (2011) 1216–1222.
[32] Z. Nemati, J. Alonso, L.M. Martinez, H. Khurshid, E. Garaio, J.A. Garcia, M.H. Phan, H. Srikanth, Enhanced magnetic hyperthermia in iron oxide nano-octopods: size and anisotropy effects, J. Phys. Chem. C 120 (2016) 8370–8379.
[33] Y. Eom, M. Abbas, H.Y. Noha, C.G. Kim, Morphology-controlled synthesis of highly crystalline Fe_3O_4 and $CoFe_2O_4$ nanoparticles using a facile thermal decomposition method, RSC Adv. 6 (2016) 15861–15867.
[34] A.G. Roca, D. Carmona, N. Miguel-Sancho, O. Bomatí-Miguel, F. Balas, C. Piquer, J. Santamaría, Surface functionalization for tailoring the aggregation and magnetic behaviour of silica-coated iron oxide nanostructures, Nanotechnol. 23 (2012) 155603.
[35] D.F. Coral, P. Mendoza Zélis, M. Marciello, M. del Puerto Morales, A. Craievich, F.H. Sánchez, M.B. Fernández van Raap, Effect of nanoclustering and dipolar interactions in heat generation for magnetic hyperthermia, Langmuir 32 (2016) 1201–1213.
[36] A.G. Roca, R. Costo, A.F. Rebolledo, S. Veintemillas-Verdaguer, P. Tartaj, T. Gonzalez-Carréno, M.P. Morales, C.J. Serna, Progress in the preparation of magnetic nanoparticles for applications in biomedicine, J. Phys. D: Appl. Phys. 42 (2009) 224002.
[37] J. Carrey, B. Mehdaoui, M. Respaud, Simple model for dynamic hysteresis loop calculations of magnetic single-domain nanoparticles: application to magnetic hyperthermia optimization, J. Appl. Phys. 109 (2011) 083921.
[38] G. Salas, J. Camarero, D. Cabrera, H. Takacs, M. Varela, R. Ludwig, H. Dahring, I. Hilger, R. Miranda, M. del Puerto Morales, F.J. Teran, Modulation of magnetic heating via dipolar magnetic interactions in monodisperse and crystalline iron oxide nanoparticles, J. Phys. Chem. C 118 (2014) 19985–19994.
[39] B. Luigjes, S.M.C. Woudenberg, R. de Groot, J.D. Meeldijk, H.M. Torres Galvis, K.P. de Jong, A.P. Philipse, B.H. Erné, Diverging geometric and magnetic size distributions of iron oxide nanocrystals, J. Phys. Chem. C 115 (2013) 14598–14605.
[40] L. Lartigue, P. Hugounenq, D. Alloyeau, S.P. Clarke, M. Lévy, J.-C. Bacri, R. Bazzi, D.F. Brougham, C. Wilhelm, F. Gazeau, Cooperative organization in iron oxide multi-core nanoparticles potentiates their efficiency as heating mediators and MRI contrast agents, ACS Nano 6 (2012) 10935–10949.
[41] I. Conde-Leboran, D. Baldomir, C. Martinez-Boubeta, O. Chubykalo-Fesenko, M. del Puerto Morales, G. Salas, D. Cabrera, J. Camarero, F.J. Teran, D. Serantes, A single picture explains diversity of hyperthermia response of magnetic nanoparticles, J. Phys. Chem. C 119 (2015) 15698–15706.
[42] M. Ma, Y. Wu, J. Zhou, Y. Sun, Y. Zhang, N. Gu, Size dependence of specific power absorption of Fe_3O_4 particles in AC magnetic field, J. Magn. Magn. Mater. 268 (2004) 33–36.
[43] P. de la Presa, Y. Luengo, M. Multigner, R. Costo, M.P. Morales, G. Rivero, A. Hernando, Study of heating efficiency as a function of concentration, size, and applied field in γ–Fe_2O_3 nanoparticles, J. Phys. Chem. C 116 (2012) 25602–25610.
[44] M. Filippousi, M. Angelakeris, M. Katsikini, E. Paloura, Il. Efthimiopoulos, Y. Wang, D. Zamboulis, G. Van Tendeloo, Surfactant effects on the structural and magnetic properties of iron oxide nanoparticles, J. Phys. Chem. C 118 (2014) 16209–16217.
[45] E. Wetterskog, C.-W. Tai, J. Grins, L. Bergström, G. Salazar-Alvarez, Anomalous magnetic properties of nanoparticles arising from defect structures: topotaxial oxidation of $Fe_{1-x}O|Fe_{3-\delta}O_4$ core|shell nanocubes to single-phase particles, ACS Nano 7 (2013) 7132–7144.
[46] Y. Bao, M. Beerman, A.B. Pakhomov, K.M. Krishnan, Controlled crystalline structure and surface stability of cobalt nanocrystals, J. Phys. Chem. B 109 (2005) 7220–7222.
[47] J. Salafranca, J. Gazquez, N. Pérez, A. Labarta, S.T. Pantelides, S.J. Pennycook, X. Batlle, M. Varela, Surfactant organic molecules restore magnetism in metal-oxide nanoparticle surfaces, Nano Lett. 12 (2012) 2499–2503.
[48] C.L. Dennis, A.J. Jackson, J.A. Borchers, R. Ivkov, A.R. Foreman, J.W. Lau, E. Goernitz, C. Gruettner, The influence of collective behavior on the magnetic and heating properties of iron oxide nanoparticles, J. Appl. Phys. 103 (2008) 07A319.
[49] A. Sánchez-Iglesias, M. Grzelczak, T. Altantzis, B. Goris, J. Pérez-Juste, S. Bals, G. Van Tendeloo, S.H. Donaldson Jr., B.F. Chmelka, J.N. Israelachvili, L.M. Liz-Marzán, Hydrophobic interactions modulate self-assembly of nanoparticles, ACS Nano 6 (2012) 11059–11065.
[50] C. Moya, X. Batlle, A. Labarta, The effect of oleic acid on the synthesis of $Fe_{3-x}O_4$ nanoparticles over a wide size range, Phys. Chem. Chem. Phys. 17 (2015) 27373–27379.
[51] W. Kim, C.-Y. Suh, S.-W. Cho, K.-M. Roh, H. Kwon, K. Song, I.-J. Shon, A new method for the identification and quantification of magnetite-maghemite mixture using conventional X-ray diffraction technique, Talanta 94 (2012) 348–352.
[52] Y.-K. Sun, M. Ma, Y. Zhang, N. Gu, Synthesis of nanometer − size maghemite particles from magnetite, Colloids Surf. A 245 (2004) 15–19.
[53] B.D. Cullity, Introduction to Magnetic Materials, Addison − Wesley, Massachusetts, 1972.
[54] B.D. Plouffe, D.K. Nagesha, R.S. DiPietro, S. Sridhar, D. Heiman, S.K. Murthy, L.H. Lewis, Thermomagnetic determination of Fe_3O_4 magnetic nanoparticle diameters for biomedical applications, J. Magn. Magn. Mater. 323 (2011) 2310–2317.
[55] R.W. Chantrell, J. Popplewell, S.W. Charles, Measurements of particle size distribution parameters in ferrofluids, IEEE Trans. Magn. 14 (1978) 975–977.
[56] The Chantrell's equation is derived from the Langevin function for noninteracting magnetic nanoparticles with the log-normal size distribution. ms and Ms are the saturation magnetizations of the nanoparticles and bulk phase respectively (in emu/g), χi is the initial magnetic susceptibility measured at low magnetic fields, and 1/H0ex (in 1/Oe) is obtained by extrapolating M to zero at high fields in the region where the relationship between M and reciprocal of the magnetic field is a straight line.
[57] E. Lima Jr., A.L. Brandl, A.D. Arelaro, G.F. Goya, Spin disorder and magnetic anisotropy in Fe_3O_4 nanoparticles, J. Appl. Phys. 99 (2006) 083908.
[58] J.Y. Jiang, S. Mørup, Correlation between peak and median blocking temperatures by magnetization measurement on isolated ferromagnetic and antiferromagnetic particle systems, Nanostruct. Mater. 9 (1997) 375–378.
[59] C. Djurberg, P. Svedlindh, P. Nordblad, M.F. Hansen, F. Bødker, S. Mørup, Dynamics of an interacting particle system: evidence of critical slowing down, Phys. Rev. Lett. 79 (1997) 5154–5157.
[60] J. Sun, Y. Zhang, Z. Chen, J. Zhou, N. Gu, Fibrous aggregation of magnetite nanoparticles induced by a time − varied magnetic field, Angew. Chem. Int. Ed. 46 (2007) 4767–4770.
[61] J.-P. Fortin, C. Wilhelm, J. Servais, C. Ménager, J.-C. Bacri, F. Gazeau, Size-sorted anionic iron oxide nanomagnets as colloidal mediators for magnetic hyperthermia, J. Am. Chem. Soc. 129 (2007) 2628–2635.